Smart Materials and
Structures

PAPER

Vibration transmissibility of piezoelectric quasi-zero stiffness metastructures with linear and nonlinear shunts

To cite this article: Kaijun Yi *et al* 2025 *Smart Mater. Struct.* **34** 045008

IOP Publishing
Smart Materials and Structures

Smart Mater. Struct. **34** (2025) 045008 (16pp)
https://doi.org/10.1088/1361-665X/adc909

Vibration transmissibility of piezoelectric quasi-zero stiffness metastructures with linear and nonlinear shunts

Kaijun Yi[1,*], **Shouqian Jiang**[1], **Ivana Kovacic**[2], **Jianlei Zhao**[1] and **Rui Zhu**[1]

[1] School of Aerospace Engineering, Beijing Institute of Technology, Beijing 100081, People's Republic of China
[2] Faculty of Technical Science, Centre of Excellence for Vibro-Acoustic Systems and Signal Processing, University of Novi Sad, Novi Sad 21000, Serbia

E-mail: kaijun.yi@bit.edu.cn

Received 13 January 2025, revised 15 March 2025
Accepted for publication 3 April 2025
Published 10 April 2025

Abstract

This study investigates the dynamics of a piezoelectric quasi-zero stiffness metastructure controlled by linear and nonlinear shunts. An equivalent lumped-mass model of the metastructure with shunts is developed. The absolute displacement transmissibility of the metastructure is calculated analytically and numerically, with results from both methods showing strong agreement. Optimized shunt parameters are determined based on the linear transfer function of the system under base excitation, and the effects of linear and nonlinear shunts on the transmissibility are thoroughly analyzed. At a relatively high excitation level, the interaction between the resonant shunts and the metastructure splits the transmissibility curve into two branches, significantly reducing the peaks of the primary branch. When the excitation amplitude exceeds a threshold, severe detuning occurs, causing the separated branches to merge, which diminishes the control effectiveness of the shunts. Nonlinear shunts exhibit a higher critical detuning excitation amplitude compared to linear ones, as their resonance frequencies expand with increasing excitation amplitude. The metastructure's resonance frequency increases at a faster rate than that of the nonlinear shunt, eventually causing the shunt to detune. By appropriately reducing the inductance to raise the shunt's resonance frequency, the branches of the transmissibility curve can be effectively separated again, thereby reducing the amplitudes of the main branch.

Keywords: metastructure, piezoelectric shunt, quasi-zero stiffness, nonlinearity, vibration isolation

1. Introduction

Vibration transmissibility issues can greatly compromise the functionality and reliability of equipment, especially when dealing with low-frequency disturbances that are notoriously difficult to manage. A practical approach to minimize these issues is to use isolators that serve as 'barriers' between the source of vibration and the affected system. The performance of such isolators heavily depends on their ability to combine high static stiffness, which is necessary for load-bearing, with low dynamic stiffness, which is crucial for isolation efficiency at lower frequencies. One potential solution is a quasi-zero stiffness (QZS) isolator. These isolators are specifically

---

[*] Author to whom any correspondence should be addressed.

designed to have a zero stiffness at the equilibrium position and nonlinear stiffness characteristic elsewhere, which allows them to effectively handle complex dynamic requirements while providing the necessary support and maintaining the isolation performance.

A widely recognized strategy for designing QZS isolators is to combine positive stiffness and negative stiffness components [1]. Positive stiffness elements are responsible for providing strong load-bearing support, while negative stiffness elements counterbalance this stiffness to achieve a QZS effect. This configuration enables isolators to operate at the frequencies much lower than those of standard linear systems. Several designs for QZS isolators have been proposed, and they differ mutually with respect to the way how the negative stiffness elements are realized. A commonly adopted method employs oblique springs to produce mechanisms with negative stiffness [2–9]. Additionally, the buckling properties of beams and plates have been extensively utilized as a basis for creating QZS isolators [10–12]. Other innovative techniques include the use of cams and rotors to introduce negative stiffness [13, 14], and the application of nonlinear magnetic forces, which can serve to create positive or negative stiffness [15, 16] or directly achieve the QZS effect [17].

Curved beams have recently been employed as fundamental components for developing a novel class of structured isolators, referred to as QZS metastructures. Unlike conventional QZS isolators, these metastructures can be incorporated into existing structures, thereby considerably minimizing the additional mass typically introduced by separate isolators in practical applications. Cai *et al* [18], Fan *et al* [19], and Dalela *et al* [20] utilized curved beams to achieve negative stiffness and paired semi-circular beams to achieve positive stiffness for constructing QZS metastructures. Additionally, a single cosine-shaped curved beam can be used to directly create QZS unit cells, enabling the design of lightweight and compact metastructures [21, 22].

However, whether in conventional QZS isolators or newly introduced metastructures, significant vibration peaks remain evident near the resonant frequencies. While employing materials with high damping can help mitigate these peaks, it may also compromise vibration isolation efficiency in the working frequency ranges, ultimately reducing the overall performance of the isolators. On the other hand, when the excitation amplitude is high, the peak of the transmissibility curve shifts significantly to the right due to the effects of hardening nonlinearity, potentially leading to jumping phenomena. To overcome these issues, in recent years, a dynamic vibration absorber (DVA) [23–27] or a nonlinear energy sink (NES) [28–30] is introduced into a QZS isolator. The DVA or NES can absorb part of the vibration energy of the isolator, therefore, considerably reducing amplitude of the nonlinear resonant peak, even linearizing the behavior of the isolator near the resonance in some cases. The resonance frequency of a QZS isolator or a metastructure usually is very low, which means to reduce such a low-frequency peak, a large mass in the DVA or NES is needed. As a result, a DVA or a NES is difficult to be integrated with a QZS metastructure due to a very limited space [22].

Recently, we have proposed to introduce piezoelectric materials with linear resonant shunts into a QZS metastructure to mitigate a resonant peak [31]. The linear resonant shunts generate narrow-band large damping to reduce the resonant peak of the metastructure and have nearly no influence on the isolation performance within the working frequency band. In this previous work, we assumed that the excitation amplitude is low and that the metastructure behaves as a linear system. In the current work, we extend the analyzes to investigate the influences of the shunts on the vibration transmissibility when nonlinearity is strong. To do so, we consider both linear and nonlinear resonant shunts. A linear resonant shunt connected to a piezoelectric patch usually is composed of inductors and resistors [32]. By combing a nonlinear capacitor or a nonlinear inductor into the linear resonant shunt, one can obtain a nonlinear resonant shunt [33–35]. In practice, a nonlinear resonant shunt can be realized using synthetic inductors [36], voltage source [37] or operational amplifiers [38]. In recent years, digital circuits with delicately designed control algorithms have been proposed to obtain synthetic impedances [39, 40]. They can be used to obtain linear resonance at very low frequencies [41–46]. Also, nonlinear resonant shunts have been realized using digital circuits [47–50]. Digital circuits can achieve very large inductance, which is typically limited to millihenries when using analog components.

In this work, we mainly focus on the interaction between the nonlinear QZS metastructure and nonlinear shunts when excitation level increases and explain the underlying physics. To present the methodologies and findings of this work, this manuscript, besides the Introduction, contains four additional sections. Section 2 introduces the physical model of the proposed piezoelectric QZS (Piezo-QZS) metastructure with shunts. Section 3 presents a mathematical model to analyze the nonlinear dynamics of the metastructure with linear and nonlinear shunts, providing also a method to optimize the shunts when the system is excited by the base motion. In section 4, we compare the control effects of linear and nonlinear shunts on the absolute displacement transmissibility of the metastructure. Finally, section 5 summarizes the key findings of this study.

2. Physical model of a piezoelectric QZS metastructure with shunts

Figure 1(a) shows an example of the proposed nonlinear Piezo-QZS metastructure. The basic functional unit cell of the metastructure is shown in figure 1(b). The unit cell is composed of a cosinusoidal beam supported by thick frames. On the surfaces of the curved beam, piezoelectric micro-fiber composite (MFC) patches are attached, each of the patch is connected to a shunt, the components of which will be specified in section 3. The shape of the curved beam in its fabricated state is:

$$\bar{w} = h/2\left[1 - \cos\left(2\pi x/l\right)\right] \tag{1}$$

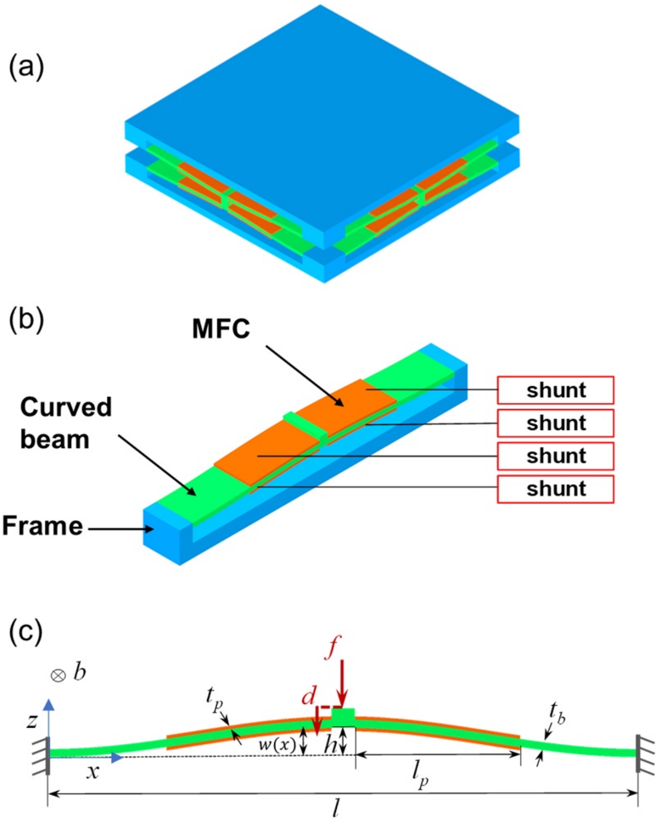

Figure 1. (a) A 3D Piezo-QZS metastructure; (b) a Piezo-QZS unit cell with shunts; (c) geometry of the piezo-curved beam.

in which, l is the span, h is the initial apex height, as illustrated in figure 1(c). We also define b as the width of the beam and t_b as the thickness.

For a MFC patch, the span, width and thickness of it are l_p, b and t_p, respectively. The patches cover the surfaces from $0.23l$ to $0.77l$ on the curved beam with a gap of $0.02l$ in the middle. Such geometry configurations of the MFC patches are optimized according to the shape of the first linear resonant mode of the curved beam in our previous work [31]. In this work we deal with the first nonlinear resonant mode. Our focus is on the influence of the shunt on the resonant peak, even though we have not adjusted the geometry and location of the patches according to the nonlinear resonant mode but adopted the design in the linear case in [31], the results in section 4 demonstrate that the MFC patches with optimized linear and nonlinear shunts can effectively reduce the amplitudes of resonances.

3. Theoretical model for dynamic analysis

In this section, we propose a theoretical model to study the dynamics of the Pizeo-QZS metastructure with linear and nonlinear shunts. First of all, a nonlinear relationship between the force applied at the center of the curved beam (see figure 1(c)) and the displacement of the central point is derived under open-circuited condition. Based on this relationship, a single degree of freedom (DOF) lumped model with linear and nonlinear stiffness is obtained as a representation of the curved beam, and another equation to describe the coupled shunts is also established.

3.1. Nonlinear force-displacement relationship of a piezo-curved beam

We assume that a force f is applied at the center of the beam, as illustrated in figure 1(c). The vertical displacement at the center of the beam is d. To find the relationship between f and d, we need to obtain the expression of the deformed shape of the beam, which is $w(x)$. In theory, the deflection of a curved beam can be approximated by superimposing the buckling modes of a clamped straight beam [51]. Given that the force is applied at the center, the curved beam's deformation will exhibit symmetry. It has also been shown that the first mode contributes the most significantly compared to higher-order terms [31]. Therefore, for simplicity, higher-order terms are disregarded. Consequently, the deformed shape of the curved beam can be approximated as:

$$w(x) = A_1\left[1-\cos\left(2\pi\frac{x}{l}\right)\right] \tag{2}$$

where A_1 is an unknown coefficient.

Now we can calculate the potential energy associated with the deformation of the beam. At this stage, the patches are assumed to be open-circuited. The total bending energy of the curved beam is:

$$\begin{aligned} u_\mathrm{b} &= 2\left\{\frac{D_\mathrm{b}}{2}\int_0^{0.23l}\left(\frac{\partial^2\overline{w}}{\partial x^2}-\frac{\partial^2 w}{\partial x^2}\right)^2\mathrm{d}x+\frac{D_\mathrm{eff}^\mathrm{oc}}{2}\int_{0.23l}^{0.49l}\left(\frac{\partial^2\overline{w}}{\partial x^2}-\frac{\partial^2 w}{\partial x^2}\right)^2\mathrm{d}x\right. \\ &\quad\left.+\frac{D_\mathrm{b}}{2}\int_{0.49l}^{0.5l}\left(\frac{\partial^2\overline{w}}{\partial x^2}-\frac{\partial^2 w}{\partial x^2}\right)^2\mathrm{d}x\right\} \\ &= \frac{\left(D_\mathrm{b}C_{11}+D_\mathrm{eff}^\mathrm{oc}C_{21}+D_\mathrm{b}C_{31}\right)}{l^3}\left(\frac{h^2}{4}-A_1h+A_1^2\right) \end{aligned} \tag{3}$$

where $D_\mathrm{b} = E_\mathrm{b}I_\mathrm{b}$ and E_b is the Young's modulus of the host beam and $I_\mathrm{b} = bt_\mathrm{b}^3/12$; D_eff is the equivalent bending stiffness of the part of the curved beam covered by the MFC patches when the patches are open-circuited, and the expression for which is given by:

$$D_\mathrm{eff}^\mathrm{oc} = \frac{bE_\mathrm{p}^\mathrm{oc}\left[\left(t_\mathrm{b}+2t_\mathrm{p}\right)^3-t_\mathrm{b}^3\right]+E_\mathrm{b}bt_\mathrm{b}^3}{12} \tag{4}$$

with $E_\mathrm{p}^\mathrm{oc} = E_\mathrm{p}^\mathrm{sc}/1-k_{31}^2$ being the Young's modulus of the patch under open-circuited condition, E_p^sc is the Young's modulus of the patch under short-circuited condition, $k_{31} = d_{31}\sqrt{E_\mathrm{p}^\mathrm{sc}/\varepsilon_{33}}$ is the electromechanical coupling coefficient of the material. The other constants in equation (3) are $C_{11} = 1.9983\pi^4$, $C_{21} = 1.8419\pi^4$ and $C_{31} = 0.1598\pi^4$.

In addition to bending, the curved beam is also subjected to horizontal compression from the lateral force due to the horizontal constraint boundaries. To calculate the compression energy, we assume that the deformation of the MFC matches the deformation of the base beam to which it is attached, and that the two pairs of piezoelectric patches undergo identical deformation due to their symmetric configuration. After several steps, the compression energy of the entire piezo-curved beam is expressed as:

$$u_{\mathrm{s}} = \frac{b}{8l^3}\left(15.38E_{\mathrm{p}}^{\mathrm{oc}}t_{\mathrm{p}}D_{11}^2 + E_{\mathrm{b}}t_{\mathrm{b}}D_{21}^2\right)\left(-\frac{h^2}{4} + A_1^2\right)^2 \tag{5}$$

with $D_{11} = 0.5795\pi^2, D_{21} = 2\pi^2$.

The work done by the external force will also contribute to the potential energy of the deflected beam, and it is calculated as follows:

$$u_f = -f \cdot d = -f \cdot \left[\bar{w}\left(\frac{l}{2}\right) - w\left(\frac{l}{2}\right)\right] = -f \cdot (h - 2A_1). \tag{6}$$

The total potential energy of the piezo-curved beam under applied force is:

$$u_{\mathrm{tot}} = u_{\mathrm{b}} + u_{\mathrm{s}} + u_{\mathrm{f}}. \tag{7}$$

By applying the principle of a minimal potential energy, the following force-displacement relationship is derived:

$$\begin{aligned} f = {} & \frac{b}{32l^3}\left(15.38E_{\mathrm{p}}^{\mathrm{oc}}t_{\mathrm{p}}D_{11}^2 + E_{\mathrm{b}}t_{\mathrm{b}}D_{21}^2\right)\left(d^3 - 3hd^2 + 2h^2d\right) \\ & + \frac{\left(D_{\mathrm{b}}C_{11} + D_{\mathrm{eff}}^{\mathrm{oc}}C_{21} + D_{\mathrm{b}}C_{31}\right)}{2l^3}d. \end{aligned} \tag{8}$$

From equation (8), we can also determine the conditions that the material and geometric parameters of the piezo-curved beam must satisfy to achieve the QZS characteristic. For simplicity, we introduce the following dimensionless parameters:

$$F = \frac{fl^3}{E_{\mathrm{b}}Ih}, \Delta = \frac{d}{h}, P = \frac{t_{\mathrm{p}}}{t_{\mathrm{b}}}, Q = \frac{h}{t_{\mathrm{b}}}, S = \frac{E_{\mathrm{p}}^{\mathrm{oc}}}{E_{\mathrm{b}}}.$$

Using the above dimensionless parameters, equation (8) is rewritten as:

$$\begin{aligned} F = {} & \frac{3}{8}AQ^2\Delta\left(\Delta - \frac{3}{2} + \sqrt{\frac{1}{4} - \frac{4B}{3AQ^2}}\right) \\ & \times \left(\Delta - \frac{3}{2} - \sqrt{\frac{1}{4} - \frac{4B}{3AQ^2}}\right) \end{aligned} \tag{9}$$

where $A = 15.38SPD_{11}^2 + D_{21}^2, B = C_{11} + C_{21} + C_{31} + SC_{21}\left(8P^3 + 12P^2 + 6P\right)$.

By differentiating equation (9) with respect to Δ, one can obtain the nonlinear stiffness:

$$K = \frac{9Q^2A}{8}\Delta^2 - \frac{9Q^2A}{4}\Delta + \frac{3Q^2A}{4} + \frac{B}{2}. \tag{10}$$

The QZS characteristic is achieved when the beam's minimal stiffness approaches zero. This minimal stiffness occurs at the static equilibrium position where $\Delta = 1$, and it can be represented as:

$$K_{\min} = \frac{B}{2} - \frac{3}{8}AQ^2. \tag{11}$$

Letting $K_{\min} \approx 0$, the condition that parameters P, Q, and S must satisfy to achieve the QZS property is derived as follows:

$$4B - 3AQ^2 \approx 0. \tag{12}$$

The accuracy of equation (12) has been well verified in our previous work [31].

3.2. Governing equations

To analyze the dynamic responses of the Piezo-QZS metastructure, we assume that the applied load causes the curved beam to be compressed to the horizontal position (figure 2(a)). Since the focus is on the dynamic responses near the first resonance frequency, a simplified single DOF model is typically used to represent the loaded metastructure in this context [20, 22]. The single DOF model is illustrated in figure 2(b). It contains a mass M, a nonlinear spring k_{nl} and a dashpot c. The motion of the base is $z_{\mathrm{b}}(t)$ and that of the mass is $z_{\mathrm{t}}(t)$. The relative displacement between the base and top mass is $z(t) = z_{\mathrm{t}}(t) - z_{\mathrm{b}}(t)$. When the MFC patches are all open-circuited, the stiffness of the nonlinear spring can be derived by substituting $d = h + z$ into equation (8), which is:

$$f = k_1^{\mathrm{oc}}z + k_3^{\mathrm{oc}}z^3 + \frac{D_{\mathrm{b}}C_{11} + D_{\mathrm{eff}}^{\mathrm{oc}}C_{21} + D_{\mathrm{b}}C_{31}}{2l^3}h \tag{13}$$

where

$$\begin{cases} k_1^{oc} = \dfrac{D_bC_{11} + D_{eff}^{oc}C_{21} + D_bC_{31}}{2l^3} - \dfrac{b}{32l^3}\left(15.38E_p^{oc}t_pD_{11}^2 + E_bt_bD_{21}^2\right)h^2 \\ k_3^{oc} = \dfrac{b}{32l^3}\left(15.38E_p^{oc}t_pD_{11}^2 + E_bt_bD_{21}^2\right) \end{cases} \tag{14}$$

To reduce the first resonant peak, a shunt is connected to each MFC patch. Habib *et al* [52, 53] pointed out that the best vibration mitigation effects can be achieved if a nonlinear absorber governed by a similar equation to the primary system is used. In other words, the order of nonlinearity of the dynamic absorber should be equal to that of the host system. Returning to this work, as can be seen in equation (13), the nonlinearity of the curved beam is cubic. Therefore, a nonlinear capacitance C_{nl} with cubic nonlinearity is used. The shunt also contains a linear inductor L and a linear resistor R in series to the nonlinear capacitance. The curved beam and the shunt

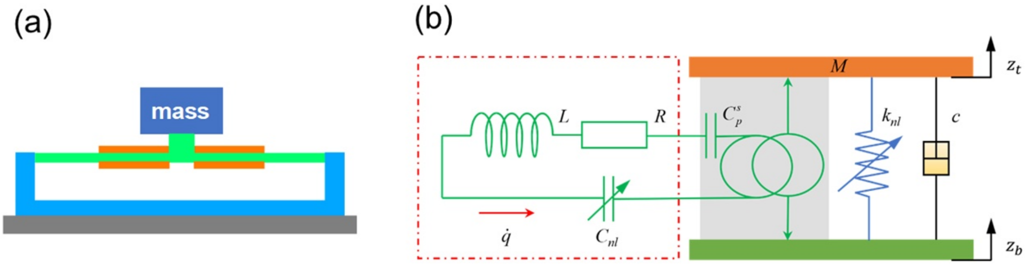

Figure 2. An equivalent theoretical model of the metastructure with nonlinear shunt. (a) The curved beam is compressed to its equilibrium position, (b) the nonlinear shunt composes a linear inductor L, a linear resistor R and a nonlinear capacitor C_{nl}.

is coupled through the MFC patch, and we use θ to represent the electromechanical coupling term in the single DOF model. Therefore, the governing equation for the relative displacement of the mass is:

$$M\ddot{z}+c\dot{z}+k_1^{\mathrm{oc}}z+k_3^{\mathrm{oc}}z^3-\theta q=-M\ddot{z}_{\mathrm{b}} \tag{15}$$

here, q is the charge in the shunt, the governing equation for which is:

$$L\ddot{q}+R\dot{q}+\frac{1}{C_{\mathrm{nl}}}q^3=V_{\mathrm{p}} \tag{16}$$

with V_{p} being the voltage of the patch. This voltage is induced by the mechanical deformation in accordance with:

$$V_{\mathrm{p}}=\theta z-\frac{1}{C_{\mathrm{p}}^{\mathrm{s}}}q \tag{17}$$

where $C_{\mathrm{p}}^{\mathrm{s}}=\left(1-k_{31}^2\right)A_{\mathrm{p}}\varepsilon_{33}/t_{\mathrm{p}}$ is the intrinsic capacitance of the patch, A_{p} is the area of the top surface of the patch. Combining equations (16) and (17), we derive:

$$L\ddot{q}+R\dot{q}+\frac{1}{C_{\mathrm{p}}^{\mathrm{s}}}q+\frac{1}{C_{\mathrm{nl}}}q^3-\theta z=0. \tag{18}$$

Obviously, it can be seen that equation (18) has the exact form as equation (15).

Based on equations (15) and (18), it is clear that the displacement of the top mass depends not only on the mechanical properties of the curved beam but also on the values of the components in the shunt. However, before using equations (15) and (18) to analyze the dynamic responses, we must first derive the expression for the electromechanical coupling term θ, which is provided below.

We consider that all the patches are short-circuited, which means $V_{\mathrm{p}}=0$. According to equations (15) and (17), we have:

$$\begin{cases} M\ddot{z}+c\dot{z}+k_1^{oc}z+k_3^{oc}z^3-\theta q=0 \\ 0=\theta z-\dfrac{1}{C_p^s}q \end{cases} \tag{19}$$

Eliminating the variable q in the first equation of equation (19):

$$M\ddot{z}+c\dot{z}+\left(k_1^{\mathrm{oc}}-\theta^2C_{\mathrm{p}}^{s}\right)z+k_3^{\mathrm{oc}}z^3=0. \tag{20}$$

Therefore,

$$\theta^2=\frac{k_1^{\mathrm{oc}}-k_1^{\mathrm{sc}}}{C_{\mathrm{p}}^{\mathrm{s}}} \tag{21}$$

where k_1^{sc} is the linear stiffness of the equivalent nonlinear spring when all the MFC patches are short-circuited. It can be obtained by replacing $E_{\mathrm{p}}^{\mathrm{oc}}$ and $D_{\mathrm{eff}}^{\mathrm{oc}}$ with $E_{\mathrm{p}}^{\mathrm{sc}}$ and $D_{\mathrm{eff}}^{\mathrm{sc}}$ in equation (14).

By substituting the expressions of k_1^{oc} and k_1^{sc} into equation (21), we have:

$$\theta^2=\left\{\frac{bC_{21}\left[\left(t_{\mathrm{b}}+2t_{\mathrm{p}}\right)^3-t_{\mathrm{b}}^3\right]}{24l^3}-\frac{bh^2h_{\mathrm{p}}D_{11}^2}{2.08l^3}\right\}\cdot\frac{E_{\mathrm{p}}^{\mathrm{oc}}-E_{\mathrm{p}}^{\mathrm{sc}}}{C_{\mathrm{p}}^{\mathrm{s}}}. \tag{22}$$

Until now, all the parameters in equations (15) and (18) are identified, with the exception of those belonging to the shunt, which will be optimized using a method proposed in section 3.4.

3.3. *Transmissibility*

We assume that the base moves harmonically $z_{\mathrm{b}}=Z_{\mathrm{b}}\cos\left(\omega t\right)$. The frequency response of the top mass can be calculated by solving equations (15) and (18). Given the fact that the system contains the cubic (Duffing) stiffness nonlinearity and that it is base excited, the analytical response cannot be found analytically in the exact form [54] and one needs to utilize the approximate approach. For the sake of that, it is assumed herein that the response is predominantly such that it contains the first harmonic only, while the higher ones are neglected. Such assumption is verified numerically for each of the cases studied.

The relative displacement between the mass and base and the charge in the shunt is assumed as:

$$\begin{aligned} z&=Z\cos\left(\omega t+\varphi_1\right) \\ q&=Q\cos\left(\omega t+\varphi_2\right) \end{aligned} \tag{23}$$

here, φ_1 and φ_2 are the phase differences between the excitation and responses.

Substituting equation (23) into equations (15) and (18), the governing equations can be rewritten into:

$$
\begin{cases}
\begin{bmatrix} -M\omega^2 Z\cos\left(\omega t+\varphi_1\right) - c\omega Z\sin\left(\omega t+\varphi_1\right) \\ +k_1^{oc}Z\cos\left(\omega t+\varphi_1\right) + k_3^{oc}Z^3\cos^3\left(\omega t+\varphi_1\right) - \theta Q\cos\left(\omega t+\varphi_2\right) \end{bmatrix} = M\omega^2 Z_b\cos\omega t \\
\begin{bmatrix} -L\omega^2 Q\cos\left(\omega t+\varphi_2\right) - R\omega Q\sin\left(\omega t+\varphi_2\right) \\ +\dfrac{1}{C_p^s}Q\cos\left(\omega t+\varphi_2\right) + \dfrac{1}{C_{nl}}Q^3\cos^3\left(\omega t+\varphi_2\right) - \theta Z\cos\left(\omega t+\varphi_1\right) \end{bmatrix} = 0
\end{cases}
\tag{24}
$$

By setting the terms related to the first harmonic on both sides of the above equations equal, and omitting the terms related to higher harmonics, i.e. applying the first-order harmonic balance method (HBM), we obtain the following equations:

$$
\begin{cases}
-M\omega^2 Z + k_1^{oc}Z + \dfrac{3}{4}k_3^{oc}Z^3 - \theta Q\cos\left(\varphi_2-\varphi_1\right) - M\omega^2 Z_b\cos\varphi_1 = 0 \\
-c\omega Z + \theta Q\sin\left(\varphi_2-\varphi_1\right) - M\omega^2 Z_b\sin\varphi_1 = 0 \\
-L\omega^2 Q + \dfrac{1}{C_p^s}Q + \dfrac{3}{4}\dfrac{1}{C_{nl}}Q^3 - \theta Z\cos\left(\varphi_2-\varphi_1\right) = 0 \\
R\omega Q + \theta Z\sin\left(\varphi_2-\varphi_1\right) = 0
\end{cases}
\tag{25}
$$

By eliminating the variables φ_1 and φ_2, we obtain:

$$
\begin{cases}
\left(-LQ\omega^2 + \dfrac{Q}{C_p^s} + \dfrac{3}{4}\dfrac{Q^3}{C_{nl}}\right)^2 + R^2Q^2\omega^2 - \theta^2 Z^2 = 0 \\
\omega^2\left(cZ + \dfrac{RQ^2}{Z}\right)^2 + \left[-MZ\omega^2 + k_1^{oc}Z + \dfrac{3}{4}k_3^{oc}Z^3 - \dfrac{Q}{Z}\left(-LQ\omega^2 + \dfrac{Q}{C_p^s} + \dfrac{3}{4}\dfrac{Q^3}{C_{nl}}\right)\right]^2 - M^2\omega^4 Z_b^2 = 0
\end{cases}
\tag{26}
$$

When the amplitude Z_b and frequency ω of the base excitation are given, by solving the equations in equation (26), we can obtain the amplitude Z of the relative displacement of the mass and the amplitude Q of the charge. The absolute displacement transmissibility from the base to the mass then can be calculated through:

$$
T = 20\log\left|\frac{z+z_\mathrm{b}}{z_\mathrm{b}}\right| = 20\log\frac{\sqrt{Z^2+Z_\mathrm{b}^2+2ZZ_\mathrm{b}\cos\varphi_1}}{Z_\mathrm{b}}
\tag{27}
$$

in which,

$$
\cos\varphi_1 = \frac{-MZ\omega^2 + k_1^{\mathrm{oc}}Z + \frac{3}{4}k_3^{\mathrm{oc}}Z^3 - \frac{Q^2}{Z}\left(-L\omega^2 + \frac{1}{C_\mathrm{p}^\mathrm{s}} + \frac{3}{4}\frac{1}{C_\mathrm{nl}}Q^2\right)}{MZ_\mathrm{b}\omega^2}.
$$

To verify these approximate analytical results, we also solve the exact governing equations (15) and (18) in time domain numerically by using the fourth-order Runge-Kutta Method (RKM). The excitation is also taken as $z_\mathrm{b} = Z_\mathrm{b}\cos\left(\omega t\right)$ and the frequency of it is swept over a certain frequency range. We obtain the time-domain response of the mass and calculate the transmissibility based on:

$$
T = 20\log\left|\frac{\mathrm{RMS}\left(z_\mathrm{t}\right)}{\mathrm{RMS}\left(z_\mathrm{b}\right)}\right|
\tag{28}
$$

where RMS stands for the root mean square operation on a signal.

3.4. Optimization of the shunt

To minimize the resonant peak around the system's first resonance, it is necessary to optimize the values of L, R and C_nl in the shunt. Several methods for this optimization have been proposed in previous investigations, including approaches outlined in [35, 36]. However, in those works, the studied systems are excited by forces, while in this work, the system is base excitated. This difference makes the transfer function of the corresponding linear system different. As a result, the optimized values of L and R in previous works cannot be directly used here since they are calculated using the transfer function. Therefore, we need to determine the optimal parameters specifically suited for our system.

For the values of L and R, they usually are optimized by ignoring the nonlinear terms in both the mechanical and electrical parts (namely, $k_3^{\mathrm{oc}} = 0, C_{\mathrm{nl}} = \infty$) [35]. For such a linear system, we can use the so-called *two equal peaks method* to find the optimal values [55]. For the corresponding linear system of equations (15) and (18), under the harmonic excitation of the base, the transfer function of the linear system is:

$$\begin{aligned} H(\omega) &= \frac{Z+Z_{\mathrm{b}}}{Z_{\mathrm{b}}} \\ &= \frac{k_1^{\mathrm{oc}}\left(-L\omega^2 + i\omega R + 1/C_{\mathrm{p}}^{\mathrm{s}}\right) - \theta^2}{\left(-M\omega^2 + k_1^{\mathrm{oc}}\right)\left(-L\omega^2 + i\omega R + 1/C_{\mathrm{p}}^{\mathrm{s}}\right) - \theta^2}. \end{aligned} \tag{29}$$

Note that the mechanical damping is ignored in the above expression, and this approximation is valid if the damping is small [55].

The key idea of the *two equal peaks method* is to find the values of L and R to make the two peaks of the transfer function in equation (29) equal. Such values are determined in three steps. First, we use the following equation to calculate the two frequencies at where the transfer function has values independent of R:

$$|H(\omega)|_{R=0} = |H(\omega)|_{R=\infty}. \tag{30}$$

The left term in the equation is the absolute value of the transfer function when $R = 0$, and the right one is the absolute value of the transfer function when the MFC patch is open-circuited. By solving equation (30), we can obtain two frequencies, ω_1 and ω_2, and they depend on L.

Then, the optimal value of L can be obtained through:

$$|H(\omega_1)|_{R=0} = |H(\omega_2)|_{R=0}. \tag{31}$$

Lastly, for the optimal value of R, the following conditions must be satisfied:

$$\frac{\partial |H(\omega)|}{\partial \omega}\Big|_{\omega=\omega_1} = 0, \quad \frac{\partial |H(\omega)|}{\partial \omega}\Big|_{\omega=\omega_2} = 0. \tag{32}$$

Usually, from the first and second equations in equation (32), two different R will be obtained, namely, R_1 and R_2, and we can choose the optimal value of R to be $(R_1 + R_2)/2$.

It should be pointed out that the explicit expressions for the optimized values of L and R can be derived using equations (30)–(32), but they will be very cumbersome and not needed as such. In this work, we calculate the optimal L and R by numerically solving equations (30)–(32).

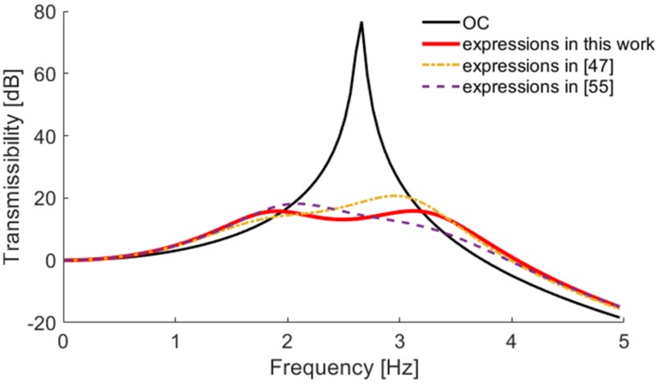

Figure 3. Comparison of the effects of linear shunts with parameters optimized by using different methods.

To verify the effects of the optimized L and R, we use the parameters in table 2 (see section 4) and ignore the nonlinear terms in both the mechanical and electrical parts. We compare the transmissibility curves between the case with optimized linear shunt (obtained using equations (30)–(32)) and the case under the open-circuited condition in figure 3. Clearly it is observed that the values of L and R derived from equations (30)–(32) can achieve two equal resonant peaks, which means that the optimized control effect is obtained. We have also calculated the transmissibility curves when values of L and R are obtained using the expressions in [47, 55]. It is clearly confirmed that those formulas cannot be directly used in our case with the excitation stemming from the motion of the base as it is apparent that the amplitude of two peaks are not equal.

For the nonlinear capacitance, it can be determined according to the principle of similarity [36, 52, 53]. Adopting this rule to our system, the nonlinear stiffness ratio between the shunt and metastructure is approximately $2\left(\frac{L}{M}\right)^2$. The optimized value of the nonlinear capacitance therefore is:

$$C_{\mathrm{nl}} = \frac{M^2}{2L^2 k_3^{\mathrm{oc}}}. \tag{33}$$

Substituting the optimal values calculated via equations (30)–(33) into equations (15) and (18) and solving the equations using the methods in section 3.3, we can obtain the transmissibility of the metastructure with shunts.

4. Results and discussion

To study the control effects of the shunts, here, we use a metastructure with one piezo-curved beam as an example. The geometry and material parameters of the curved beam are designed using equation (12), and they are detailed in table 1. The QZS characteristic of the designed beam was confirmed in [31] both numerically and experimentally.

Using the parameters in table 1, we can calculate the parameters of the theoretical model proposed in section 3, and the

Table 1. Geometric and material parameters of the piezo-curved beam.

Base beam	MFC [56]
$E = 70$ GPa	$E_p^{sc} = 32.58$ GPa
$t_b = 1.7$ mm	$d_{31} = -267 \times 10^{-12}$ C/N
$h = 2.1$ mm	$\varepsilon_{33} = 2344.4\varepsilon_0$
$l = 100$ mm	$t_p = 0.3$ mm
$b = 14$ mm	\

Table 2. Parameters of the theoretical model.

M (Kg)	c (Nsm^{-1})	k_1^{sc} (Nm^{-1})	k_1^{oc} (Nm^{-1})	k_3^{oc} (Nm^{-3})	C_p^s (nF)	θ (N/C)
21.2	7	3.95×10^3	5.87×10^3	2.27×10^{10}	89.4	1.47×10^5

corresponding results are given in table 2. Note that, the mass is chosen to be 21.2 kg to make the curved beam work within the QZS region. The damping coefficient of the beam is chosen to be $c = 7$, which results in a small modal damping ratio of approximately 1%, i.e. $\xi = \frac{c}{2M\sqrt{k_1^{oc}/M}} \approx 0.01$.

We would like to emphasize that, in order to accurately use the equivalent model proposed in section 3, the following conditions or assumptions must be met:

- The maximum absolute displacement of the curved beam should be less than a critical value. Under this condition, we can only use the first static mode to obtain the analytical expression of the nonlinear stiffness of the curved beam. For the designed metastructure in table 1, this value is about 4 mm, as illustrated in figure 3 of our previous work [31].
- The second resonance frequency of the compressed metastructure should be significantly higher than the maximum frequency under study. This allows us to model the complex structure using the first resonant mode and obtain a simplified single DOF model.
- The nonlinear responses are dominated by the primary harmonic.

In figure 4, the transmissibility curves under different excitation amplitudes are studied when the MFC patches are open-circuited. When the excitation amplitude is small (for example, $Z_b = 1 \times 10^{-6}$ m), the system behaves like a linear one. If the excitation amplitude exceeds 1×10^{-5} m, the branches and the resonance peaks of the transmission curves noticeably lean to the right, which is feature of systems with hardening stiffness nonlinearity. We also calculate the transmissibility using the RKM when $Z_b = 8 \times 10^{-5}$ m. During the numerical simulations, the frequency is swept both forward and backward, the stable results in the previous step are used as initial values in the next step. Apparently, the approximate analytical results from the HBM and numerical results from RKM match very well with each other, which demonstrates the accuracy of our methods, and provides verifications of the approximation used by assuming the response as having one harmonic dominantly, as described by equation (23).

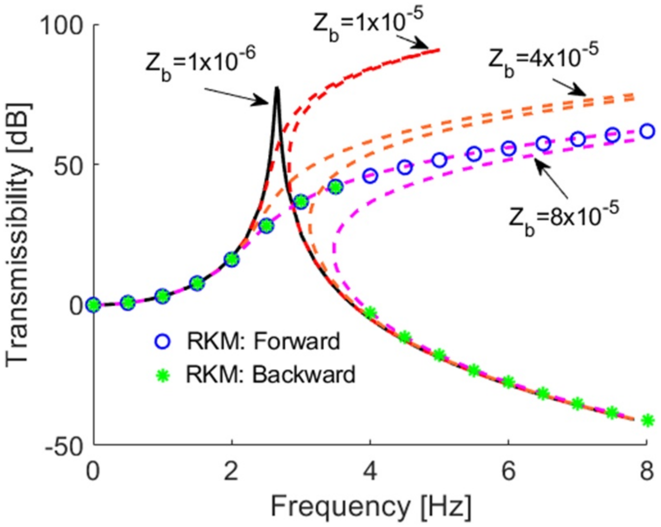

Figure 4. Transmissibility of the metastructure under the open-circuited condition corresponding to different excitation amplitudes. Lines represent results from HBM.

4.1. Comparison between linear and nonlinear shunts

First, we study the effects of linear shunts with optimal values on the resonant peak of the transmissibility curve. We compare the transmissibility curves between the cases with and without shunts, while also considering varying levels of the amplitude of base excitation. The results are illustrated in figure 5, both results from HBM and RKM are shown. At lower excitation level (figures 5(a)–(c)), it is evident that a significant outcome of the interaction between the resonant shunt and the beam is the splitting of the transmissibility curve into two branches, namely, a main branch and a detached branch (Note that, to find the solutions on the detached curves using RKM, the solutions of HBM are used as initial values). Such phenomenon has also been reported in other nonlinear systems with internal couplings, the detached curve is also called isola [57–62]. The peaks of the primary resonance curves are significantly reduced by the linear shunt. On the other hand, the shunt has minimal to no effect on the resonances corresponding to the

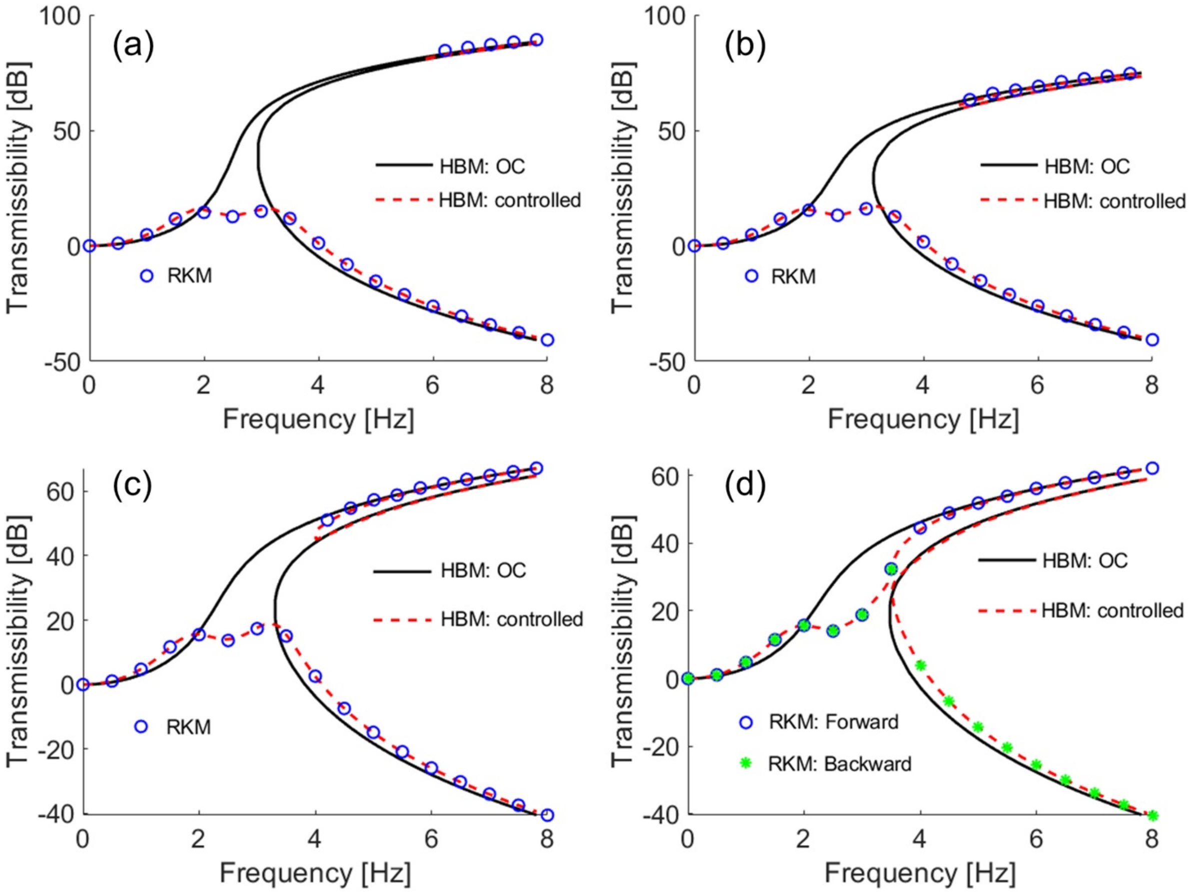

Figure 5. Effects of linear shunt with optimal values on the resonant peaks, $L = 3.38 \times 10^4$ H, $R = 4.29 \times 10^5 \Omega$. (a) $Z_b = 2 \times 10^{-5}$ m, (b) $Z_b = 4 \times 10^{-5}$ m, (c) $Z_b = 6 \times 10^{-5}$ m, (d) $Z_b = 8 \times 10^{-5}$ m.

detached curves in terms of reducing amplitudes. When the excitation amplitude exceeds a certain value ($Z_b \geqslant 8 \times 10^{-5}$ m for the system studied), the effectiveness of the linear shunt significantly diminishes, as shown in figure 5(d). The detached resonance curve is again merged with the primary (continuous) one.

To further analyze the influences of the excitation level, in figure 6, we compare the transmissibility curves under control for cases with different excitation amplitudes. When the excitation is relatively low (figure 6(a)) but the nonlinearity cannot be ignored, the nonlinear resonant peak is perfectly mitigated by the linear shunt. When the excitation amplitude exceeds 1.4×10^{-5} m, an isola is observed (figure 6(b)). As the excitation amplitude increases, the right peak of the main branch grows, and the isola extends downward to the left. As a result, the two branches merge when the excitation amplitude is greater or equal to $Z_b = 8 \times 10^{-5}$ m, and the transmissibility near the right peak is dramatically increased. These phenomena are caused by the detuning between the linear shunt and the nonlinear mechanical part, because as the excitation amplitude increases, the resonance frequency of the metastructure increases but that of the linear shunt stays unchanged.

Next, we study the effects of the nonlinear shunt with optimal values on the resonant peak. The transmissibility curves for the nonlinear cases are shown in figure 7. Like in the linear cases, when the excitation amplitude remains relatively small (figures 7(a)–(c)), the transmissibility curve is divided into two distinctive branches, and the responses of the primary branches are significantly reduced by the nonlinear shunt. When the excitation amplitude reaches $Z_b = 10 \times 10^{-5}$ m, the two branches merge.

We also compare the transmissibility curves with nonlinear shunt at different excitation levels, and the corresponding results are shown in figure 8. The details reveal a similar phenomenon observed as in the linear case: when the excitation amplitude exceeds 1.4×10^{-5} m, an isola becomes apparent; as the excitation further increases, the response amplitudes near the second peak of the main branch increases, and the detached curve becomes lower, and finally they merge with each other. This phenomenon indicates that the nonlinear shunt will also gradually become increasingly detuned with the mechanical resonator as the excitation amplitude increases. Such detuning between the nonlinear shunt and the mechanical component has not been reported in previous studies [35,

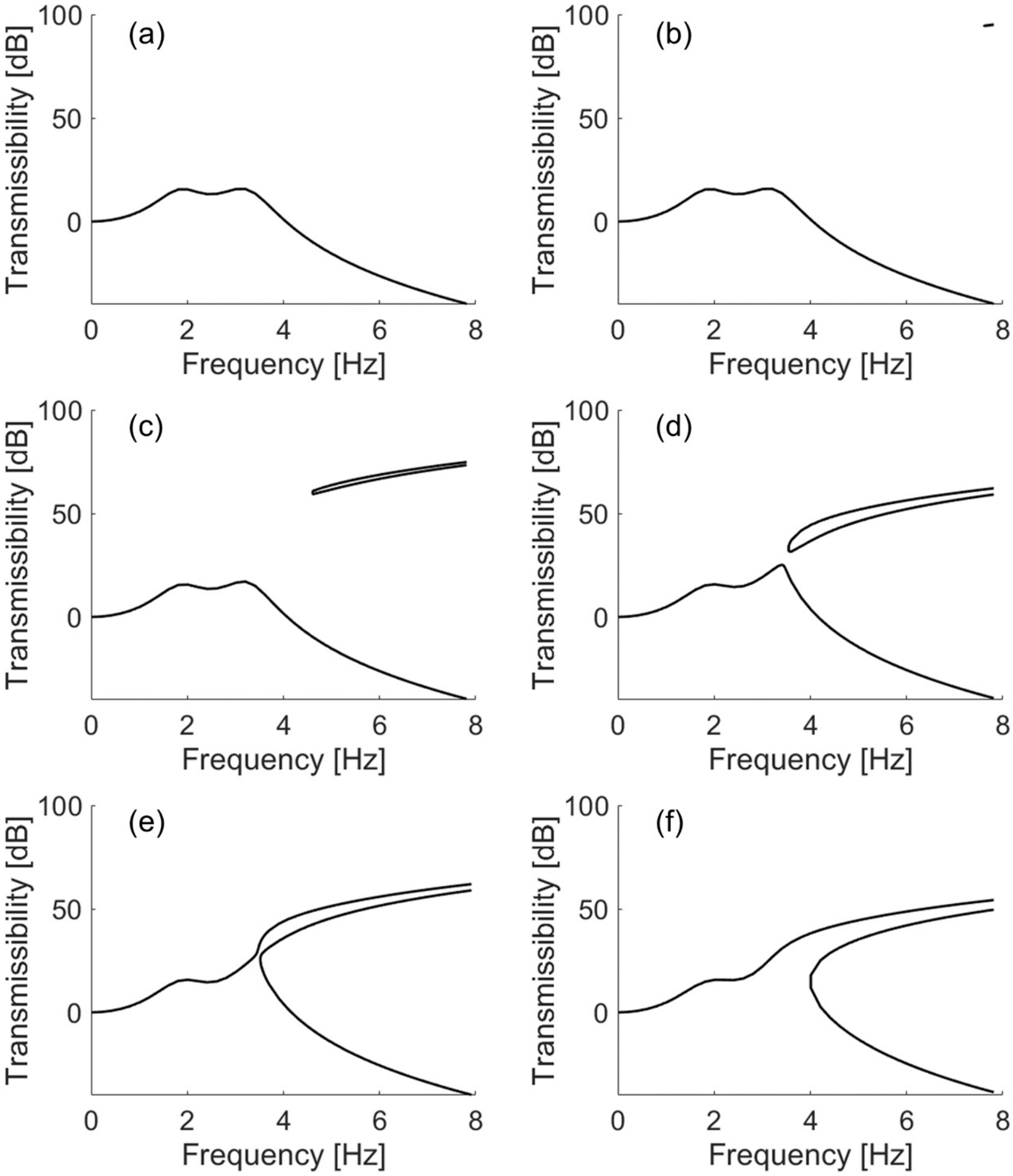

Figure 6. Comparison of the transmissibility curves for different excitation amplitudes when the piezo-curved beam is shunted with optimized linear shunt, $L = 3.38 \times 10^4$ H, $R = 4.29 \times 10^5 \Omega$. (a) $Z_b = 1 \times 10^{-5}$ m, (b) $Z_b = 1.4 \times 10^{-5}$ m, (c) $Z_b = 4 \times 10^{-5}$ m, (d) $Z_b = 7.8 \times 10^{-5}$ m, (e) $Z_b = 8 \times 10^{-5}$ m, (f) $Z_b = 12 \times 10^{-5}$ m.

36, 47], it will also make the shunt ineffective if the excitation amplitude exceeds the threshold, as illustrated in figures 8(e) and (f).

According to the results in figures 5–8, one may raise a question: what are the differences between the linear and nonlinear shunting cases? To answer this question, figure 9 compares the control effects of the linear and nonlinear shunts at the same excitation level. When the excitation amplitude is small (before the birth of the isola), the control effects of the linear and nonlinear shunts are exactly the same (figure 9(a)). As the excitation amplitude increases but remains below the critical value associated with detuning, the nonlinear shunt demonstrates better performance compared to the linear shunt. Specifically, the maximum resonant peak of the primary response curve is lower in the nonlinear case, and the gap between the two branches is more pronounced (figures 9(b) and (c)). However, before the linear shunt experiences significant detuning, the advantage of the nonlinear shunt remains relatively inconspicuous in terms of the above-mentioned control effects.

The greatest advantage of a nonlinear shunt compared with the linear counterpart is its higher critical detuning excitation amplitude. In the system studied, for the linear shunt, it will be totally detuned when $Z_b \geq 8 \times 10^{-5}$ m (figure 9(d)), but the

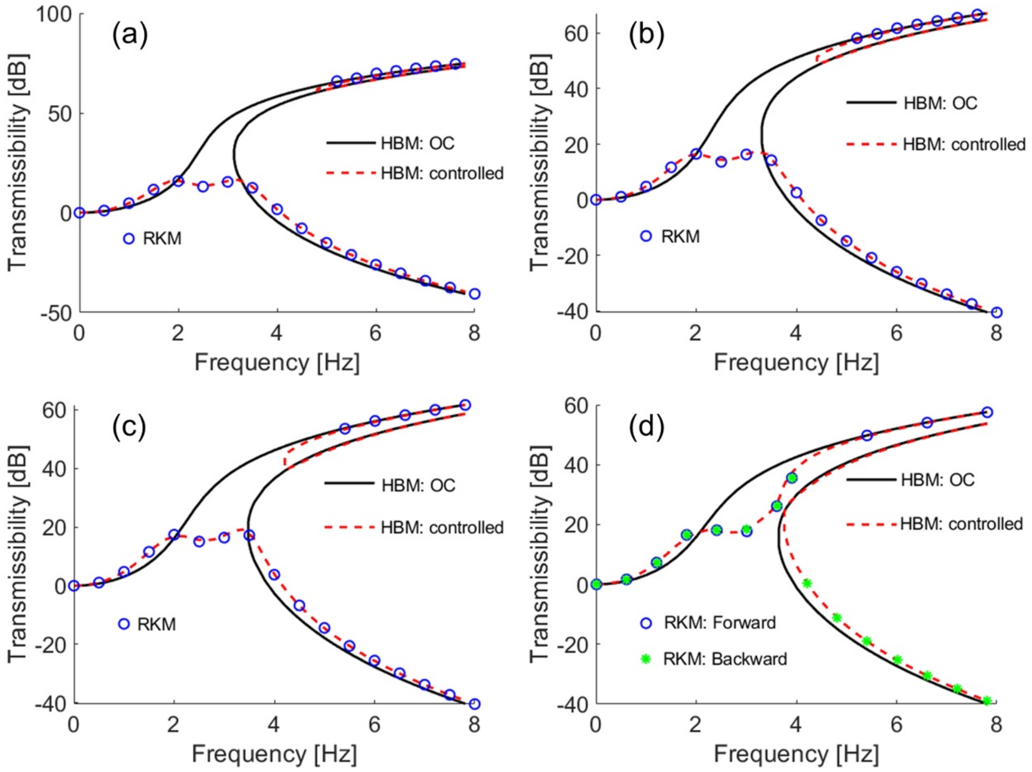

Figure 7. Effects of nonlinear shunt with optimal values on the resonant peaks, $L = 3.38 \times 10^4$ H, $R = 4.29 \times 10^5\Omega$, $C_{\mathrm{nl}} = 8.68 \times 10^{-18}$ C^3/V. (a) $Z_{\mathrm{b}} = 4 \times 10^{-5}$ m, (b) $Z_{\mathrm{b}} = 6 \times 10^{-5}$ m, (c) $Z_{\mathrm{b}} = 8 \times 10^{-5}$ m, (d) $Z_{\mathrm{b}} = 10 \times 10^{-5}$ m.

nonlinear shunt is tuned until the excitation amplitude reaches $Z_{\mathrm{b}} = 10 \times 10^{-5}$ m (figure 9(e)). The critical detuning excitation amplitude of the nonlinear shunt is 25% higher than that of the linear shunt. In both cases, when the shunts are significantly detuned, they will again have almost the same control effects on the transmissibility (figure 9(f)).

To explain why the nonlinear shunt has higher critical detuning excitation amplitude and why it will finally become detuned, we further analyze the dynamic responses of the shunt. From figure 9, we can see that as the excitation amplitude increases from 6×10^{-5} m to 10×10^{-5} m, the shunt transitions from being tuned to fully detuned. Figure 10(a) shows the voltage responses of the nonlinear shunt during this process. The linear resonance frequency of the metastructure under open-circuited condition is $\sqrt{\frac{M}{K_1^{\mathrm{oc}}}} = 2.6$ Hz. Therefore, we mainly interested in the voltage level at frequencies from 2 Hz to 3 Hz. From figure 10(a), it can be seen that the voltage amplitude is between 10 V to 40 V. Next, we disconnect the nonlinear shunt from the piezo-patch and study its dynamic responses excited by a harmonic voltage source $\mathrm{V_{in}}\cos(\omega t)$, the results are illustrated in figure 10(b). It can be observed that as the excitation level increases, the resonance frequency of the nonlinear shunt increases, while that of the linear shunt remains constant. This is why the nonlinear shunt exhibits a higher critical detuning excitation amplitude. However, since the nonlinearity of the metastructure is stronger than that of the nonlinear shunt with optimized parameters, the rate at which the shunt's resonance frequency increases is slower than that of the metastructure. As a result, the nonlinear shunt eventually becomes detuned once the excitation surpasses a certain threshold.

4.2. *A strategy for retuning shunts under conditions of large excitation amplitudes*

In this section, we propose a strategy to deal with the detuned phenomenon discussed above. As analyzed above, the detuning between the shunt and metastructure is due to the resonance frequency of the metastructure increasing at a faster rate than that of the shunt. Therefore, in the event of detuning, retuning maybe accomplished by modifying the circuit's resonance frequency through adjustments to the inductance value.

For a shunt, when it is connected to a piezoelectric patch, the linear resonant frequency of the shunt is approximately $1/\sqrt{LC_{\mathrm{s}}^{\mathrm{p}}}$. Therefore, when detuning occurs, we need to decrease the value of L to increase the resonance frequency of the shunt. A universal retuning criterion is that the retuned parameters should make the two peaks of the main branch equal again. Note that, when the value of L is changed,

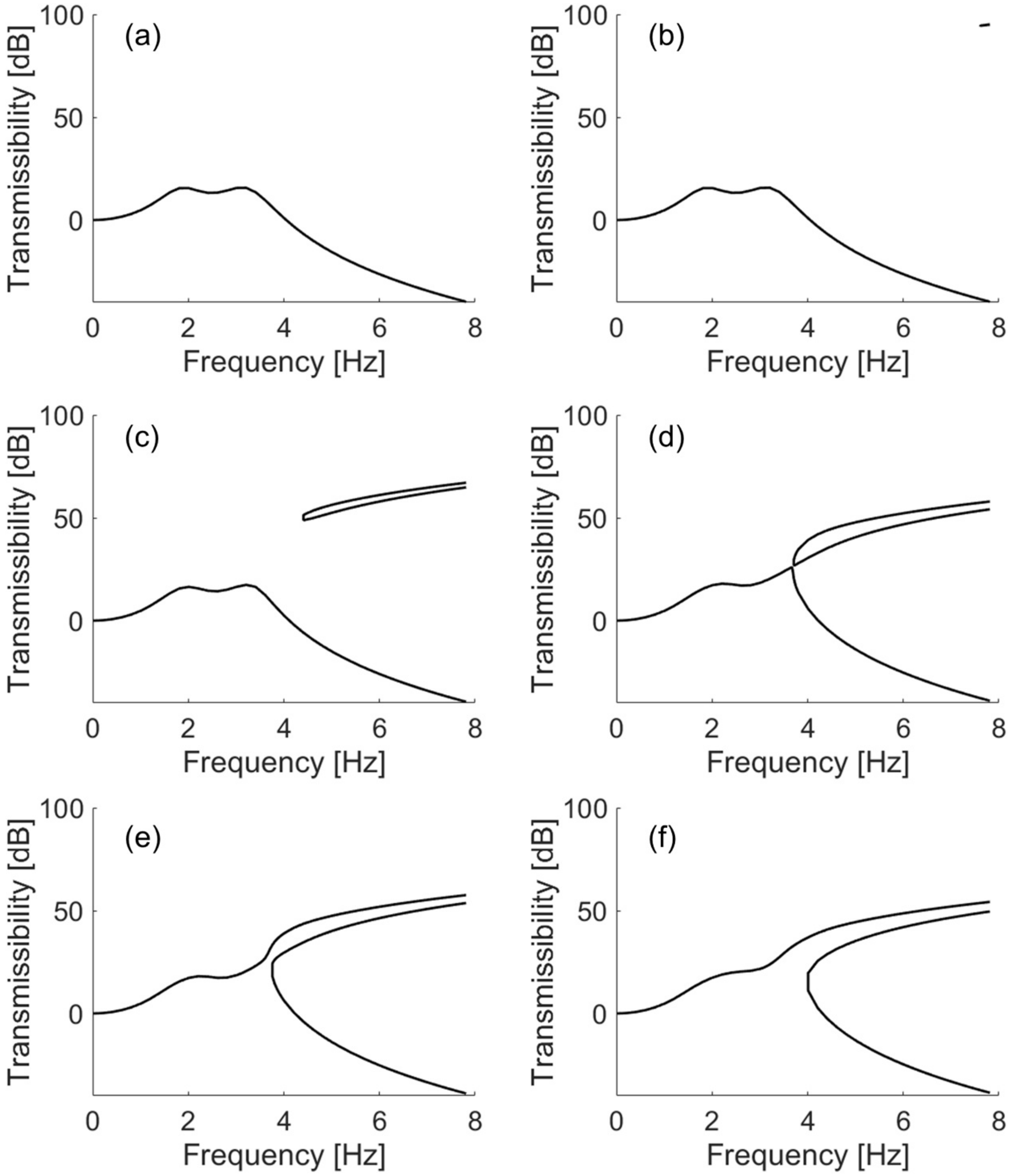

Figure 8. Comparison of the transmissibility curves for different excitation amplitudes when the piezo-curved beam is shunted with optimized nonlinear shunt, $L = 3.38 \times 10^4$ H, $R = 4.29 \times 10^5 \Omega$, $C_{\mathrm{nl}} = 8.68 \times 10^{-18}$ C^3/V. (a) $Z_{\mathrm{b}} = 1 \times 10^{-5}$ m, (b) $Z_{\mathrm{b}} = 1.4 \times 10^{-5}$ m, (c) $Z_{\mathrm{b}} = 6 \times 10^{-5}$ m, (d) $Z_{\mathrm{b}} = 9.8 \times 10^{-5}$ m, (e) $Z_{\mathrm{b}} = 10 \times 10^{-5}$ m, (f) $Z_{\mathrm{b}} = 12 \times 10^{-5}$ m.

the values of R and C_{nl} also need to be re-calculated using equations (32) and (33).

Figure 11 illustrates the effects of the retuned nonlinear and linear shunts on the transmissibility curves when $Z_{\mathrm{b}} = 10 \times 10^{-5}$ m. From both figures 11(a) and (b) we can see that, as the inductance decreases, a branch is detached from the main curve, and the right peak of the main branch becomes lower, the detached branch rises upward to the right. The optimal retuned L can be chosen as the one that makes the two peaks of the main branch equal. No doubt that this value depends on the excitation level. As shown in figure 11, when $Z_{\mathrm{b}} = 10 \times 10^{-5}$ m, a new L that is around $0.9L_{\mathrm{opt}}$ times of the original one will achieve good control effects on the primary branch in the nonlinear case (figure 11(a)). For the linear case, the retuned L is approximately $0.8L_{\mathrm{opt}}$ (figure 11(b)).

Figure 12 compares the transmissibility curves in the nonlinear and linear cases with the retuned optimal parameters for $Z_b = 10 \times 10^{-5}$ m. It can be concluded that, with proper retuning, both linear and nonlinear shunts exhibit similar control performance on the nonlinear piezo-curved beam.

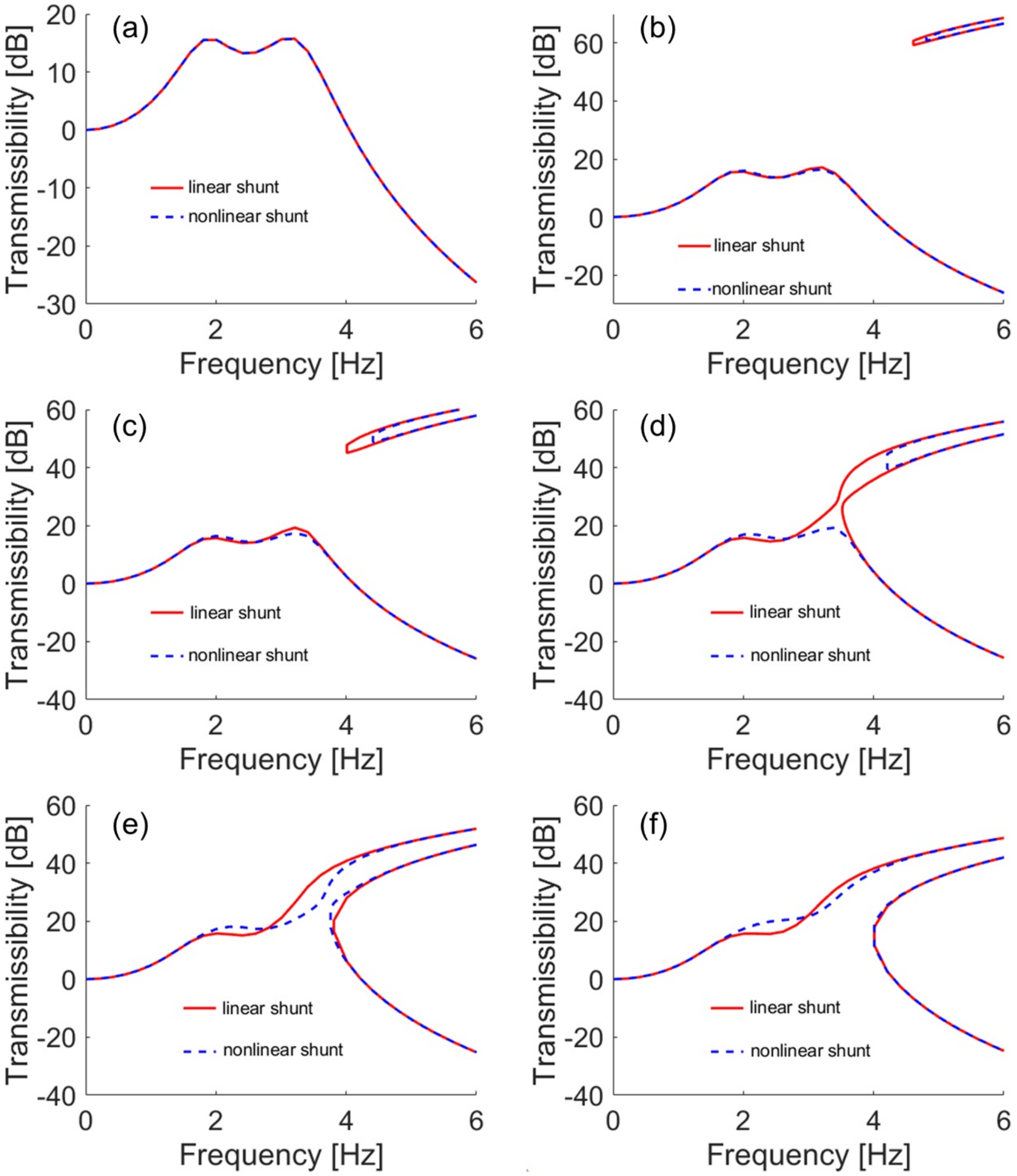

Figure 9. Comparison of the control effects of the linear and nonlinear shunts with optimal values. (a) $Z_b = 1 \times 10^{-5}$ m, (b) $Z_b = 4 \times 10^{-5}$ m, (c) $Z_b = 6 \times 10^{-5}$ m, (d) $Z_b = 8 \times 10^{-5}$ m, (e) $Z_b = 10 \times 10^{-5}$ m, (f) $Z_b = 12 \times 10^{-5}$ m.

5. Conclusion

In this work, the dynamic behavior of Piezo-QZS metastructures composed of piezo-curved beams controlled by linear and nonlinear shunts has been studied. An equivalent discrete model for the metastructure with shunts has been proposed to analyze the dynamic behavior. The absolute displacement transmissibility has been calculated both analytically and numerically, and the results obtained by using these two methods match very well with each other, verifying the hypothesis in the analytical approach about the dominance of the first harmonic in the system response. The optimized parameters of the shunts have been obtained by utilizing the linear transfer function of the system under base excitation. Using these optimized values, the effects of linear and nonlinear shunts on the transmissibility have been analyzed under different excitation amplitudes. The main findings are:

(1) The interaction between the resonant shunts and the metastructure divides the transmissibility curve into two distinct areas, with the shunts significantly reducing the peaks of the primary branch. As the excitation amplitude increases, both the linear and nonlinear shunts become detuned from the structure. Once the excitation surpasses a certain threshold, the two separate branches of the transmissibility curve converge into a single branch again. At this point, the control effectiveness of the shunts deteriorates substantially. The nonlinear shunt becomes

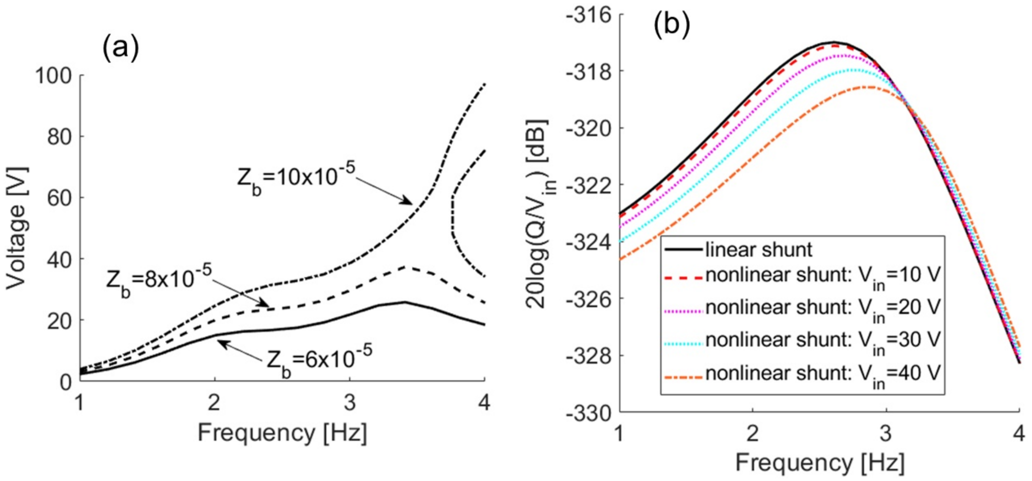

Figure 10. Voltage responses of the nonlinear shunt. (a) The shunt is connected to the metastructure excited by its base's movement, (b) the shunt is disconnected from the metastructure and is excited by a harmonic voltage source $\mathrm{V_{in}}\cos(\omega t)$. $L = 3.38 \times 10^4$ H, $R = 4.29 \times 10^5 \Omega$, $C_{\mathrm{nl}} = 8.68 \times 10^{-18}\ \mathrm{C^3/V}$ are used in all the simulations.

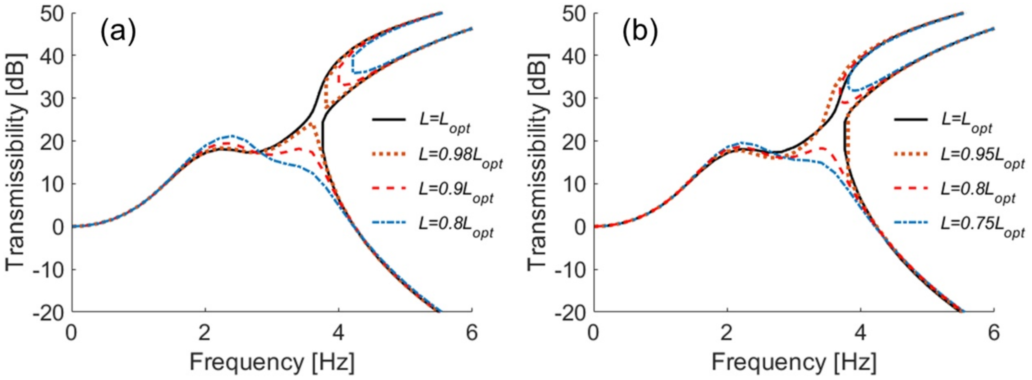

Figure 11. Influences of retuned shunt parameters on the transmissibility curve, $L_{\mathrm{opt}} = 3.38 \times 10^4$ H, R and C_{nl} in the retuned shunt are calculated using equations (32) and (33), $Z_b = 10 \times 10^{-5}$ m. (a) Nonlinear shunt, (b) linear shunt.

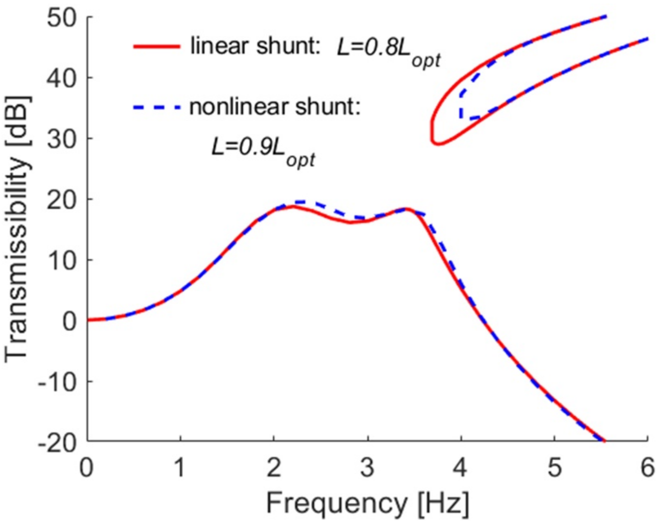

Figure 12. Comparison between the control effects of linear and nonlinear shunts with retuned parameters, $L_{\mathrm{opt}} = 3.38 \times 10^4$ H, R and C_{nl} in the retuned shunt are calculated using equations (32) and (33), $Z_b = 10 \times 10^{-5}$ m.

detuned because the increasing rate of the metastructure's resonance frequency is faster than shunt's as the excitation level raises.

(2) A strategy has been proposed to deal with the detuning. The fundamental approach involves appropriately reducing the inductance value and recalculating the other parameters within the shunts. From a physical perspective, the retuning process increases the shunt's resonance frequency to 'catch up' with the metastructure's, effectively re-separates the two branches of the transmissibility curve, which merged due to the increased excitation level.

(3) When the shunts are properly tuned to the mechanical component, both linear and nonlinear shunts show similar effectiveness in reducing transmissibility. However, the nonlinear shunt offers a distinct advantage by supporting a higher critical detuning excitation amplitude than the linear shunt, thus providing a wider operational range. This difference arises because, as the excitation level increases, the resonance frequency of the nonlinear shunt increases, whereas the resonance frequency of the linear shunt remains unchanged.

While this work primarily focuses on enhancing the vibration isolation performance of QZS metastructures, we believe the findings reached can also offer valuable insights into vibration suppression in other nonlinear systems through piezoelectric shunting techniques, which extends our findings to a higher level of applicability.

Data availability statement

All data that support the findings of this study are included within the article (and any supplementary files).

Acknowledgment

Kaijun Yi has received funding from the National Natural Science Foundation of China (NSFC) (Grant No. 12202052). The involvement of Ivana Kovacic is supported by the Ministry of Science, Technological Development and Innovation of the Republic of Serbia via the bilateral Serbia-China research project 'Noise and Vibration Isolation through Nonlinear Metastructures' (acronym NOLIMAST).

Conflict of interest

The authors declare that they have no conflict of interest.

ORCID iDs

Kaijun Yi https://orcid.org/0000-0003-2215-5479
Shouqian Jiang https://orcid.org/0009-0000-8252-9319
Ivana Kovacic https://orcid.org/0000-0002-0433-1953

References

[1] Alabudzev P 1989 *Vibration Protecting and Measuring Systems with Quasi-Zero Stiffness* (CRC Press)
[2] Cao Q, Wiercigroch M, Pavlovskaia E E, Grebogi C and Thompson J M T 2006 Archetypal oscillator for smooth and discontinuous dynamics *Phys. Rev.* E **74** 46218
[3] Carrella A, Brennan M J and Waters T P 2007 Static analysis of a passive vibration isolator with quasi-zero stiffness characteristic *J. Sound Vib.* **301** 678–89
[4] Kovacic I, Brennan M J and Waters T P 2008 A study of a nonlinear vibration isolator with a quasi-zero stiffness characteristic *J. Sound Vib.* **315** 700–11
[5] Carrella A, Brennan M J, Kovacic I and Waters T P 2009 On the force transmissibility of a vibration isolator with quasi-zero-stiffness *J. Sound Vib.* **322** 707–17
[6] Sun X, Jing X, Xu J and Cheng L 2014 A quasi-zero-stiffness-based sensor system in vibration measurement *IEEE Trans. Ind. Electron.* **61** 5606–14
[7] Lan C-C, Yang S-A and Wu Y-S 2014 Design and experiment of a compact quasi-zero-stiffness isolator capable of a wide range of loads *J. Sound Vib.* **333** 4843–58
[8] Hao Z, Cao Q and Wiercigroch M 2017 Nonlinear dynamics of the quasi-zero-stiffness SD oscillator based upon the local and global bifurcation analyses *Nonlinear Dyn.* **87** 987–1014
[9] Ding H, Ji J and Chen L 2019 Nonlinear vibration isolation for fluid-conveying pipes using quasi-zero stiffness characteristics *Mech. Syst. Signal Process.* **121** 675–88
[10] Fulcher B A, Shahan D W, Haberman M R, Conner Seepersad C and Wilson P S 2014 Analytical and experimental investigation of buckled beams as negative stiffness elements for passive vibration and shock isolation systems *J. Vib. Acoust.* **136** 031009
[11] Oyelade A O 2019 Vibration isolation using a bar and an Euler beam as negative stiffness for vehicle seat comfort *Adv. Mech. Eng.* **11** 168781401986098
[12] Shaw A, Neild S, Wagg D, Weaver P and Carrella A 2012 A nonlinear spring mechanism incorporating a bistable composite plate for vibration isolation *J. Sound Vib.* **332** 6265–75
[13] Zhou J, Wang X, Xu D and Bishop S 2015 Nonlinear dynamic characteristics of a quasi-zero stiffness vibration isolator with cam–roller–spring mechanisms *J. Sound Vib.* **346** 53–69
[14] Yao Y, Li H, Li Y and Wang X 2020 Analytical and experimental investigation of a high-static-low-dynamic stiffness isolator with cam-roller-spring mechanism *Int. J. Mech. Sci.* **186** 105888
[15] Yan G, Wu Z, Wei X, Wang S, Zou H, Zhao L, Qi W and Zhang W 2022 Nonlinear compensation method for quasi-zero stiffness vibration isolation *J. Sound Vib.* **523** 116743
[16] Yan G, Lu J, Qi H, Liu F, Yan H, Zhao L, Wu Z and Zhang W 2024 Linear and nonlinear stiffness compensation for low-frequency vibration isolation: a comparative study *Nonlinear Dyn.* **112** 5955–73
[17] Qi W, Liu F, Lu J, Zhao T, Yan H, Yan G and Zhang W 2024 Generative quasi-zero stiffness paradigm for vibration isolation by constraining the constant force with hardening boundaries *J. Sound Vib.* **589** 118548
[18] Cai C, Zhou J, Wu L, Wang K and Ouyang H 2020 Design and numerical validation of quasi-zero-stiffness metamaterials for very low-frequency band gaps *Compos. Struct.* **236** 111862
[19] Fan H, Yang L, Tian Y and Wang Z 2020 Design of metastructures with quasi-zero dynamic stiffness for vibration isolation *Compos. Struct.* **20** 112244

[20] Dalela S, Balaji P S and Jena D P 2022 Design of a metastructure for vibration isolation with quasi-zero-stiffness characteristics using bistable curved beam *Nonlinear Dyn.* **108** 1931–71

[21] Zhao W J, Wang Y T, Zhu R, Hu G K and Hu H Y 2020 Isolating low-frequency vibration via lightweight embedded metastructures *Sci. Sin.* **50** 090010

[22] Zhao J, Zhou G, Zhang D, Kovacic I, Zhu R and Hu H Y 2023 Integrated design of a lightweight metastructure for broadband vibration isolation *Int. J. Mech. Sci.* **244** 108069

[23] Liu C and Yu K 2018 A high-static–low-dynamic-stiffness vibration isolator with the auxiliary system *Nonlinear Dyn.* **94** 1549–67

[24] Li S-H, Liu N and Ding H 2020 Research on a nonlinear quasi-zero stiffness vibration isolator with a vibration absorber *Sci. Prog.* **103** 0036850420940891

[25] Liu Y, Ji W, Xu L, Gu H and Song C 2021 Dynamic characteristics of quasi-zero stiffness vibration isolation system for coupled dynamic vibration absorber *Arch. Appl. Mech.* **91** 3799–818

[26] Xing Z-Y and Yang X-D 2023 A combined vibration isolation system with quasi-zero stiffness and dynamic vibration absorber *Int. J. Mech. Sci.* **256** 108508

[27] Xing Z-Y and Yang X-D 2024 A combined vibration isolation system capable of isolating large amplitude excitation *Nonlinear Dyn.* **112** 2523–44

[28] Jiang G, Wang Y, Li F and Jing X 2021 An integrated nonlinear passive vibration control system and its vibration reduction properties *J. Sound Vib.* **509** 116231

[29] Zhang Z, Zhang Y-W and Ding H 2020 Vibration control combining nonlinear isolation and nonlinear absorption *Nonlinear Dyn.* **100** 2121–39

[30] Zeng Y-C, Ding H, Du R-H and Chen L-Q 2022 A suspension system with quasi-zero stiffness characteristics and inerter nonlinear energy sink *J. Vib. Control* **28** 143–58

[31] Jiang S, Liu Z, Yi K, Zhu R and Kovacic I 2024 Design of piezoelectric quasi—zero—stiffness metastructures for improved low—frequency vibration isolation *Smart Mater. Struct.* **33** 115017

[32] Wang M, Yi K and Zhu R 2023 Tunable underwater low-frequency sound absorption via locally resonant piezoelectric metamaterials *J. Sound Vib.* **548** 117514

[33] Agnes G S and Inman D J 1996 Nonlinear piezoelectric vibration absorbers *Smart Mater. Struct.* **5** 704

[34] Zhou B, Thouverez F and Lenoir D 2014 Essentially nonlinear piezoelectric shunt circuits applied to mistuned bladed disks *J. Sound Vib.* **333** 2520–42

[35] Soltani P and Kerschen G 2015 The nonlinear piezoelectric tuned vibration absorber *Smart Mater. Struct.* **24** 075015

[36] Lossouarn B, Deü J-F and Kerschen G 2018 A fully passive nonlinear piezoelectric vibration absorber *Phil. Trans. R. Soc.* A **376** 20170142

[37] Shami Z A, Giraud-Audine C and Thomas O 2022 A nonlinear piezoelectric shunt absorber with 2: 1 internal resonance: experimental proof of concept *Smart Mater. Struct.* **31** 035006

[38] Silva T M, Clementino M A, De Marqui C and Erturk A 2018 An experimentally validated piezoelectric nonlinear energy sink for wideband vibration attenuation *J. Sound Vib.* **437** 68–78

[39] Fleming A J, Behrens S and Moheimani S 2000 Synthetic impedance for implementation of piezoelectric shunt-damping circuits *Electron. Lett.* **36** 1525–6

[40] Matten G, Collet M, Cogan S and Sadoulet-Reboul E 2014 Synthetic impedance for adaptive piezoelectric metacomposite *Proc. Technol.* **15** 84–89

[41] Liu Z, Yi K, Sun H, Zhu R, Zhou X, Hu G and Huang G 2024 Inherent temporal metamaterials with unique time-varying stiffness and damping *Adv. Sci.* **11** 2404695

[42] Yi K, Liu Z and Zhu R 2021 Multi-resonant metamaterials based on self-sensing piezoelectric patches and digital circuits for broadband isolation of elastic wave transmission *Smart Mater. Struct.* **31** 015042

[43] Yi K, Matten G, Ouisse M, Sadoulet-Reboul E, Collet M and Chevallier G 2020 Programmable metamaterials with digital synthetic impedance circuits for vibration control *Smart Mater. Struct.* **29** 035005

[44] Sugino C, Ruzzene M and Erturk A 2020 Digitally programmable resonant elastic metamaterials *Phys. Rev. Appl.* **13** 061001

[45] Dai S, Zheng Y and Qu Y 2023 Programmable piezoelectric meta-rings with high-order digital circuits for suppressing structural and acoustic responses *Mech. Syst. Signal Process.* **200** 110517

[46] Zheng Y, Qu Y, Dai S, Chen B and Mao J 2024 Mitigating vibration and sound radiation with a digital piezoelectric meta-shell in heavy fluids *J. Sound Vib.* **573** 118221

[47] Raze G, Jadoul A, Guichaux S, Broun V and Kerschen G 2019 A digital nonlinear piezoelectric tuned vibration absorber *Smart Mater. Struct.* **29** 015007

[48] Zhang X, Yu H, He Z, Huang G, Chen Y and Wang G 2021 A metamaterial beam with inverse nonlinearity for broadband micro-vibration attenuation *Mech. Syst. Signal Process.* **159** 107826

[49] Alfahmi O, Sugino C and Erturk A 2022 Duffing-type digitally programmable nonlinear synthetic inductance for piezoelectric structures *Smart Mater. Struct.* **31** 095044

[50] Xia D, Pu X, Tong S and Xu J 2024 Piezoelectric metamaterial with digitally controlled nonlinear shunt circuit for broadband wave attenuation *Appl. Phys. Lett.* **124** 121704

[51] Qiu J, Lang J H and Slocum A H 2004 A curved-beam bistable mechanism *J. Microelectromech. Syst.* **13** 137–46

[52] Habib G and Kerschen G 2016 A principle of similarity for nonlinear vibration absorbers *Physica* D **332** 1–8

[53] Habib G, Grappasonni C and Kerschen G 2016 Passive linearization of nonlinear resonances *J. Appl. Phys.* **120** 044901

[54] Kovacic I 2020 *Nonlinear Oscillations: Exact Solutions and Their Approximations* (Springer)

[55] Thomas O, Ducarne J and Deü J-F 2011 Performance of piezoelectric shunts for vibration reduction *Smart Mater. Struct.* **21** 015008

[56] Steiger K and Mokrý P 2015 Finite element analysis of the macro fiber composite actuator: macroscopic elastic and piezoelectric properties and active control thereof by means of negative capacitance shunt circuit *Smart Mater. Struct.* **24** 025026

[57] Starosvetsky Y and Gendelman O V 2008 Response regimes of linear oscillator coupled to nonlinear energy sink with harmonic forcing and frequency detuning *J. Sound Vib.* **315** 746–65

[58] Alexander N A and Schilder F 2009 Exploring the performance of a nonlinear tuned mass damper *J. Sound Vib.* **319** 445–62

[59] Gatti G, Brennan M J and Kovacic I 2010 On the interaction of the responses at the resonance frequencies of a nonlinear two degrees-of-freedom system *Physica* D **239** 591–9

[60] Habib G, Detroux T, Viguié R and Kerschen G 2015 Nonlinear generalization of Den Hartog's equal-peak method *Mech. Syst. Signal Process.* **52** 17–28

[61] Mangussi F, Zanette D H and Ma J 2016 Internal resonance in a vibrating beam: a zoo of nonlinear resonance peaks *PLoS One* **11** e0162365

[62] Kakou P, Gupta S K and Barry O 2024 A nonlinear analysis of a Duffing oscillator with a nonlinear electromagnetic vibration absorber–inerter for concurrent vibration mitigation and energy harvesting *Nonlinear Dyn.* **112** 5847–62